INTERNATIONAL SOCIETY FOR
SOIL MECHANICS AND
GEOTECHNICAL ENGINEERING

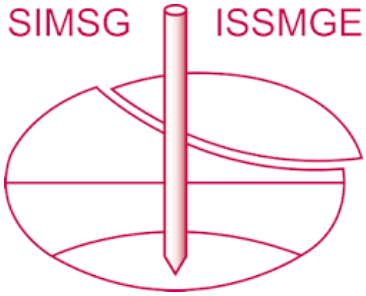

This paper was downloaded from the Online Library of the International Society for Soil Mechanics and Geotechnical Engineering (ISSMGE). The library is available here:

https://www.issmge.org/publications/online-library

This is an open-access database that archives thousands of papers published under the Auspices of the ISSMGE and maintained by the Innovation and Development Committee of ISSMGE.

The paper was published in the proceedings of the 7th International Conference on Earthquake Geotechnical Engineering and was edited by Francesco Silvestri, Nicola Moraci and Susanna Antonielli. The conference was held in Rome, Italy, 17 – 20 June 2019.

Invited papers

Taylor & Francis
Taylor & Francis Group
http://taylorandfrancis.com

Earthquake Geotechnical Engineering for Protection and Development of Environment and Constructions – Silvestri & Moraci (Eds)
© 2019 Associazione Geotecnica Italiana, Rome, Italy, ISBN 978-0-367-14328-2

Instrumentation and calibration protocols for deep, in-situ liquefaction testing with controlled blasting

A.W. Stuedlein, A. Jana, Donaldson, J.J. Batti & T.M. Evans
Oregon State University, Corvallis, Oregon, USA

ABSTRACT: Recent subduction zone earthquakes have highlighted the need to address the stress-strain response of soils subjected to long duration, high intensity ground motions. The presence of deep, liquefaction- and cyclic softening-susceptible soils in the northwestern continental United States present a significant challenge with regard to the evaluation of the potential for poor performance, ranging from the difficulty in sampling such soils to the preparation of intact, relatively undisturbed specimens for cyclic laboratory testing. In situ testing of such soils can mitigate the effects of sample disturbance while testing significantly larger volumes of soil than those associated with laboratory specimens. This paper describes the design of deep, blast-induced liquefaction experiments with a focus on the instrumentation used to make appropriate observations of the in-situ response. Efforts to quantify the deviation from true verticality of boreholes, to determine the in-situ orientation and orthogonality of geophones and accelerometers, and to calibrate specialty sensors, all of which were necessary to capture the observed response are described. Specific considerations for conducting such experiments and the procedures developed to address particular challenges associated with deep in-situ testing are emphasized.

1 INTRODUCTION

Recent subduction zone earthquakes, including the 2010 Maule, Chile and 2011 Tohoku, Japan earthquakes, have gained significant attention due to their strong intensity of shaking and long duration. The Cascadia Subduction Zone, running 1,000 km from Northern California in the south to British Columbia in the north, last ruptured on 26 January 1700 with an estimated moment magnitude of ~9.0, and produced a tsunami that resulted in thousands of deaths and casualties as far away as Japan (Atwater et al. 2004). On the basis of turbidite deposits off the Pacific Northwest coastline, Goldfinger et al. (2012) estimated that the likelihood of the next Cascadia earthquake ranges from 7 to 12% and 37 to 42% in 50 years for the northern and southern margins of the subduction zone, respectively. Accordingly, significant interest in improving seismic resiliency has increased by the owners of civil infrastructure, including departments of transportation and ports.

As part of its long-term resilience goals, the Port of Portland, located in Portland, Oregon, has determined that one of its two runways must be hardened against the vertical and lateral deformations anticipated following rupture of the Cascadia Subduction Zone and the nearby, though smaller, Port Hills fault. A portion or all of both runways lie in close proximity to the Columbia River, which has been dredged to maintain shipping freighters to depths as great as 20 m. Lateral spreading has been determined to pose a significant risk to the runways, given that the subsurface consists of dredge sand fill, medium stiff silt, and a deep deposit of medium dense sand. Prior to selecting and executing a costly ground improvement program, the Port has determined that an improved understanding of the cyclic resistance of the silt and sand deposits is warranted. Deep, in-situ blast liquefaction experiments conducted by Oregon State University served to provide a means to understand the seismic performance of these soils without the possible effects of sample disturbance, small sample-size effects, artificial

drainage conditions, and under existing mechanical, hydrogeological, and thermal conditions. This paper briefly describes the subsurface conditions and blasting test plan, followed by a detailed presentation of the instruments used and calibration procedures implemented to facilitate the deep, in-situ experiments.

2 SITE LAYOUT AND GENERAL SUBSURFACE CONDITIONS

The blast-liquefaction test site is located on the grounds of Portland International Airport, owned and operated by the Port of Portland, and situated approximately 1.2 km southeast of and aligned with the South Runway. Initial borings of the site indicated the suitability of this site for the purposes of conducting the controlled blasting experiment, as well as its sufficient distance from nearby structures. Figure 1 presents the site and exploration plan, as well as relevant components of the experiments, including blast casings, pore pressure transducers (PPTs), and velocity transducers. Note that a portion of the explorations, including those for placement of instruments and to conduct vane shear tests, are not shown in Figure 1 for clarity. The first ten blast casings (starting from the west) extended to approximately 27 m depth and were used to excite the deep instrumentation array (Figure 2), whereas the five blast casings located along the eastern end of the site extended to a depth of approximately 12 m and were used, along with the five middle casings, to excite the shallow instrumentation array. Cone penetration tests (CPTs) conducted along the array alignment, as well as mud-rotary borings performed for split-spoon sampling and penetration testing, were used to construct the subsurface model of the test site presented in Figure 2. Dredge sand and silty sand fill comprises the upper 5 to 6 m of the subsurface, and is underlain by a +/- 2 m thick layer of native loose, clean sand. Below the native sand deposit lies a 5 to 6 m thick medium stiff clayey SILT deposit with traces of sand and thin stringers of sandy SILT. Extending below the silt layer and to the depth of the explorations lies a deep deposit of medium dense, clean sand with local zones of dense sand. As indicated in Figure 2, the deep and shallow arrays were installed at depths where the CPTs indicated the most uniform conditions exist, though variations in relative density (deep array) and consistency (shallow array) were noted during sampling at the instrument locations.

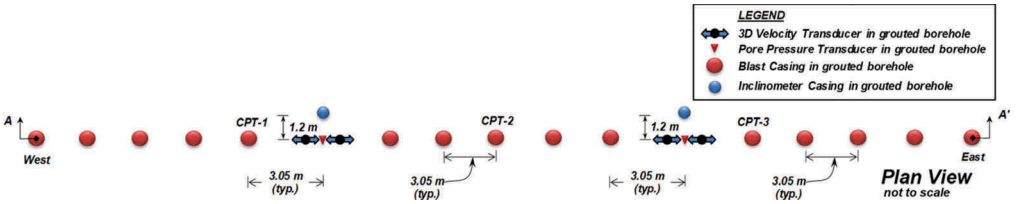

Figure 1. Site and exploration plan showing a portion of explorations (for clarity) and instrumentation arrays aligned along due East and West (representing the global coordinate system and alignment).

3 INSTRUMENTATION ARRAYS

Instruments necessary to capture the in-situ response to controlled blasting were installed within mud-rotary boreholes to form the deep and shallow array (Figure 3) and were accompanied by ground surface monitoring monuments (not discussed herein). Each array consisted of a minimum of four boreholes: (1) one to house full-depth inclinometer casing fitted with sondex settlement rings to capture post-liquefaction volumetric strain, (2) one to house the PPT string, and (3) two boreholes to place the geophone sensor packages, each of which consist of triaxial velocity transducers and a six-axis accelerometer gyroscope to capture static tilt. Figure 3 presents the intended array geometry, designed to allow deduction of the change in shear modulus and excess pore pressure with imposed

shear strain following the approach implemented by Cox et al. (2009) and van Ballegooy et al. (2015). Note that instruments were placed with minor deviations from that intended. Due to the pre-installation uncertainty of borehole deviation, sensor packages were suspended from inclinometer casings to assist in determining the post installation locations, the determination of which was guided by the adjacent full-depth inclinometer casing that accompanied each array. Sensor packages and PPTs were installed with the aid of weights to allow placement through the heavy drilling fluid specified and to plumb the sensors under gravity. Each type of instrumentation, and the installation thereof, required careful calibration in order to ensure that accurate voltage-to-amplitude conversions could be obtained and that the location and orientation of each instrument could be accurately ascertained. The remainder of this paper focuses on the instrumentation used and calibration protocols implemented to meet the experimental goals.

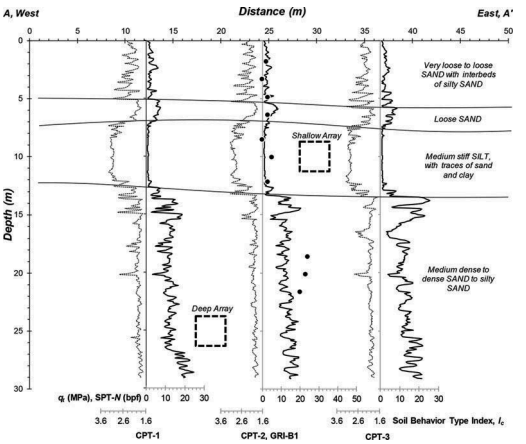

Figure 2. Subsurface cross-section A-A' showing a portion of the explorations (for clarity) and depth and extent of the deep and shallow arrays used to observe the response to controlled blasting.

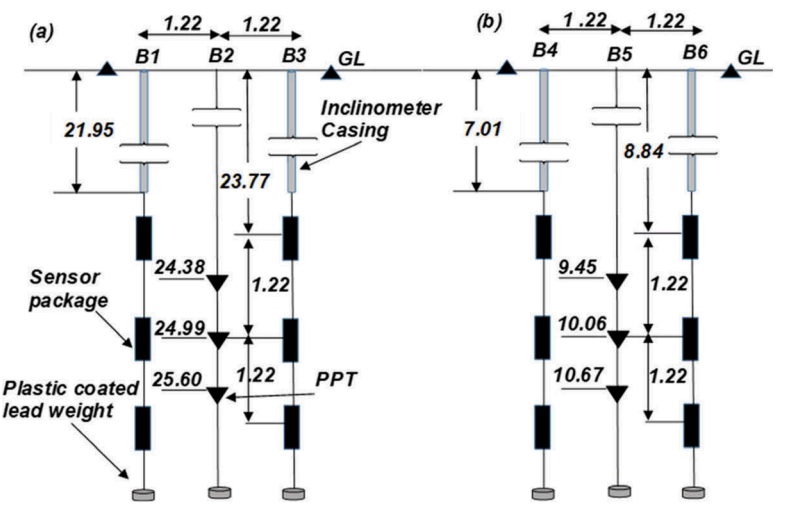

Figure 3. Elevation view of the planned (a) deep sensor array, and (b) shallow sensor array. For clarity, boreholes housing inclinometer casing with sondex rings and surface sensors are not shown here.

4 INSTRUMENTATION AND CALIBRATION PROTOCOLS

4.1 *Pore Pressure Transducers (PPTs)*

Each instrumented array was accompanied by three PPTs to observe the static pore pressure, the hydrodynamic (i.e., *p*-wave induced) and residual (i.e., s-wave induced) excess pore pressure due to blasting, and the dissipation of excess pore pressure. Rollins et al. (2005) described the desired qualities of PPTs used in blast-liquefaction studies, and recommendations therein were followed during selection of the model PPT used herein. The PPTs used were Model Unik 5000 PMP5034-TA-A3-CA-H0-PF, manufactured by GE Measurement and Control, which were determined to perform suitably in controlled blasting studies by Gianella and Stuedlein (2017). The PPT is an amplified pressure transducer capable of measuring pressure between 0 and 5.2 MPa, and withstand blast pressures of up to 20.7 MPa. The frequency response of the PPT is up to 3.5 kHz and can sustain wide temperature range of -55 to 125°C (GE Measurement 2014).

Each PPT was placed within an acrylic housing to withstand anticipated blast pressures and to prevent soil and the bentonite-cement grout mix from entering the diaphragm chamber of the PPT. To facilitate communication of pore pressures during blasting, and based on previous experience (e.g., Cox 2006; Gianella and Stuedlein 2017), two sintered, porous bronze filters were set within the housing at the location of the PPT tip where it senses the pressure. The filters were boiled for 10 minutes to remove entrapped air and assembled, along with the PPT, within the housing underwater and secured with a membrane to maintain saturation prior to placement and calibration.

Calibration of the PPTs was performed within a water-filled, 19.8 m long inclinometer casing set within a test shaft at the Geotechnical Engineering Field Research Site (GEFRS) on the OSU Campus. PPTs were placed in the inclinometer casing while maintaining saturation, and lowered to bottom of the casing and the initial static head monitored at sampling rate of 50 Hz. Thereafter, the PPT was raised in 1.5 m increments and the head observed for approximately 30 s prior to raising to the next measurement depth. Figure 4a indicates the response of one PPT during the calibration process when the PPT was taken out from the casing. The average voltage for each depth was computed and used to develop the voltage to pressure calibration relationship, which was linear and unique for each sensor. Table 1 presents the individual calibration equations and demonstrates, in view of the fitted coefficients and intercepts, the significant need to calibrate each PPT individually. Furthermore, it was determined that the PPTs exhibited sufficient deviation from the manufacturer calibration factors so to disregard their use.

4.2 *Geophone sensor packages*

Observation of body wave velocities and the development of strain and reduction in shear modulus during controlled blasting was facilitated with the geophone sensor packages. Each sensor package (Figure 5) was fitted with three geophones and a six-axis accelerometer

Table 1. Excitation-to-pressure calibration functions for PPTs.

PPT	Calibration Equation (Excitation, V to Pressure, u (kPa)	R^2
1	$u = 1041.2557\ V + 10.1946$	0.99999
2	$u = 1039.9900\ V + 8.2572$	0.99999
3	$u = 1041.0373\ V + 8.6863$	0.99999
4	$u = 1039.0437\ V + 13.2819$	0.99999
5	$u = 1042.2058\ V + 8.8506$	0.99999
6	$u = 1040.2892\ V + 16.6266$	0.99983

gyroscope. The geophones selected were 28 Hz Geospace Technologies Model GS-14-L9 with 31% damping, whereas the accelerometer-gyroscope was a Generic brand Model GY-521 MPU-6050. Due to their specialty purpose, careful calibration protocols were developed for each sensor. The sensitivity curves, which relate excitation voltage to velocity, were determined for each of the 42 geophones used in this study. The geophone test setup (Figure 5a) consisted of a MEMS accelerometer, an amplifier, an oscilloscope, and data acquisition system (DAQ), electromagnetic shaker (i.e., sound driver), and signal generator. The speaker vibrated at selected frequencies with acceleration and velocity time histories captured by the MEMS accelerometer (in g) and geophone (in volts), respectively, both of which were fixed to the speaker using wax.

During calibration, up to 15 sinusoids between 10 and 300 Hz were generated using the electromagnetic shaker and signal generator for assessment and comparison to the manufacturer sensitivity curve. Signal amplitudes were adjusted to achieve a clear waveform, inspected using the oscilloscope, and an appropriate signal-to-noise ratio. The average voltage and g amplitudes were recorded using the DAQ; the acceleration time histories were then integrated for comparison to the geophone-based velocity time histories and compared to the voltage

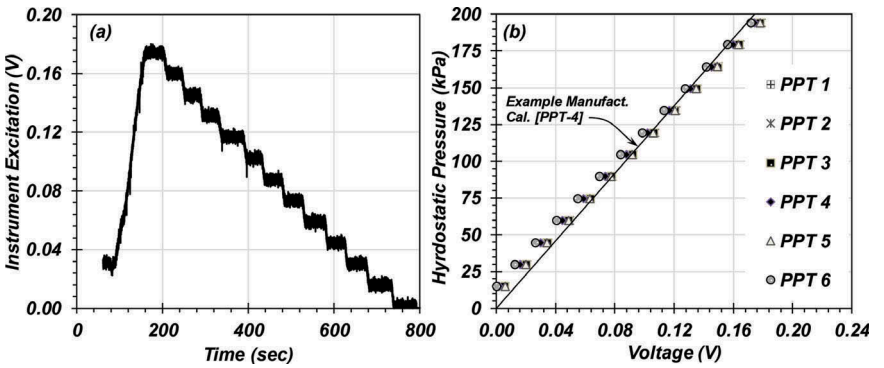

Figure 4. Pore pressure transducer calibration, including: (a)_voltage time history for PPT 4, and (b) voltage to hydrostatic pressure relationships indicating PPT-specific responses.

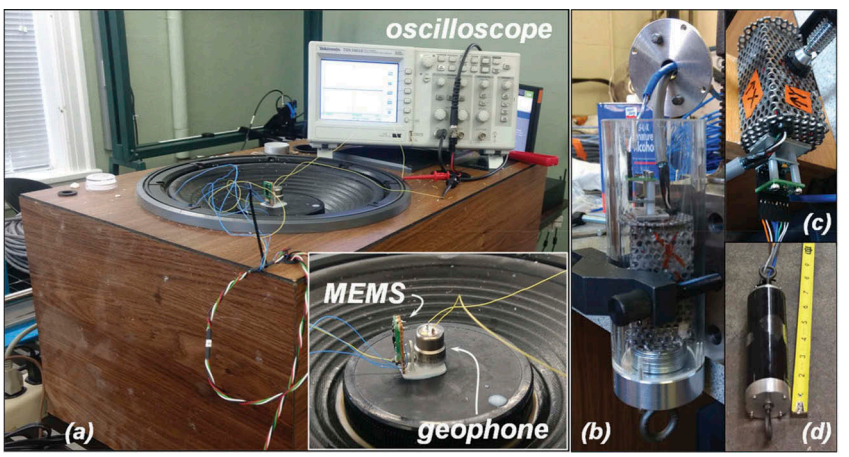

Figure 5. Geophone sensor package calibration and production: (a) geophone and MEMS calibration setup, (b) acrylic housing with weighted geophone frame (bottom) and MEMS and IMU (top) prior to placement of epoxy, (c) geophone frame housing with MEMS and IMU prior to placement, and (d) completed geophone sensor package.

excitation to produce the sensitivity curve. Figure 6 presents the resulting sensitivity curves and the manufacturer-provided curve for comparison. In general, frequencies equal to or larger than 160 Hz appear to deviate from the relationship provided by the manufacturer, although lower frequencies do appear similar in general shape. However, the deviation in the observed sensitivities from the manufacturer-supplied curve for frequencies in the vicinity of 28 Hz was significant. In this study, signal components with frequency smaller than 100 Hz were converted to velocity using their individual sensitivity curves, whereas the Geospace recommended sensitivity of 0.0236 V/mm/s were used for larger frequencies.

4.3 *Inclinometer calibration and observed borehole deviation*

Owing to the need to quantify the initial, as well as changes in, body wave speed within the instrumented array, determining the locations of the geophone sensor packages was deemed critical. Therefore, out-of-plumb deviations of the boreholes were observed using inclinometer surveys of inclinometer casing installations. The MEMS-based Geodaq i6 in-place inclinometer was used to perform the borehole deviation surveys, and consisted of two types of interchangeable modules: the INC6-R24 and INC6-R28. Module INC6-R24 has four dual-axis MEMS sensors spaced equally over the 2.44 m length, whereas the INC6-R28 module has eight dual-axis MEMS sensors evenly distributed over its length. The MEMS sensors allow monitoring of gravity in two directions and is able to measure angular deviations of 0.004° for inclinations of up to 30° (Geodaq 2014).

Manufacturer calibration of in-place inclinometers are usually sufficient for change detection, such as monitoring of unstable slopes or laterally-loaded deep foundations. However, when monitoring borehole deviation, the baseline zero-tilt sensor signals (in percent of gravity) must be carefully assessed owing to their inherent electro, mechanical and thermo-mechanical noise. A 4.89 m tall calibration frame fitted with 10 centering boxes was constructed and plumbed to allow placement of inclinometer casing and the in-place inclinometer and observation of the zero-tilt MEMS excitation for calibration purposes. Prior to placement of the inclinometer, the inclinometer casing was plumbed and leveled by adjusting screws sequentially in each of the centering boxes. Baseline MEMS data were observed using Geodaq Controller Module Version 4 (GCM4) data acquisition system by taking the average of four 30 s readings with a 10 Hz sampling rate. This process was repeated for 2 minutes to establish more reliable baseline reading of each sensor. Table 2 presents sample calibration results, including the average, standard deviation, and coefficient of variation (COV) of the first MEMS inclination sensor of each inclinometer module used in the study. Comparison of the mean and COV in zero-tilt gravitation indicates that each sensor exhibits different gravitational sensitivity and uncertainty, and that the magnitude of gravitation is significantly different than that expected with a fully-plumbed inclinometer (i.e., 1*g*). While these calibration

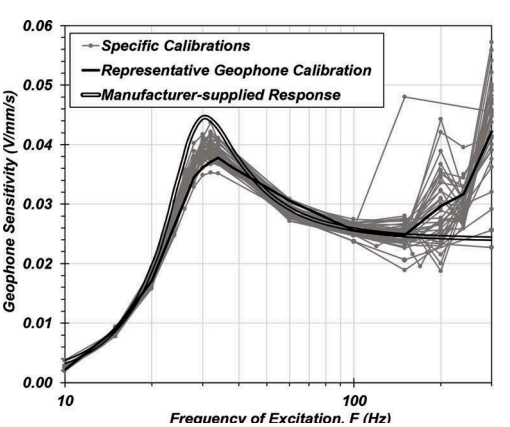

Figure 6. Comparison of observed geophone sensitivity curves to manufacturer-supplied sensitivity curve.

constants are of little concern for change detection applications, it proved critical for the assessment of borehole verticality and velocity transducer location determination.

Approximately one month after the installation of inclinometer casings in the field, the in-place inclinometer was lowered to the bottom of the casing and the tilt observed. Borehole deviation was indicated by a gravitational shift compared to the baseline, zero-tilt gravitational constant (e.g., Table 2). The lateral deviation of the borehole with depth was calculated using the cumulative sum of the borehole deviation starting from the ground surface. Figure 7a presents the lateral deviation with respect to local coordinates (X, Y) of the inclinometer casing. In this study, the X direction of the global coordinate system was chosen equal to the GPS-determined east-west array direction; therefore, compass readings of the axes of the inclinometer casing were used to correct the deviations to the global coordinate system (Figure 7b). The maximum lateral deviation of the boreholes was approximately 200 mm, equal to the diameter of the typical tri-cone drill bit, and the maximum deviation increased with the depth of the borehole.

Instrument strings were suspended from the base of the inclinometer casings, and were allowed to self-plumb under gravity (assisted by the weights as described earlier). The lateral shift of the instruments beneath the inclinometer casing was estimated in consideration of their tilt, detected using the Inertial Measurement Unit (IMU) sensor (discussed below), which provides tilt in local lateral (X, Y) directions. Table 3 presents the tilt of each sensor package in the lateral direction, and indicates that all of the sensors appear nearly plumb (*n.b.*, three of the IMUs did not appear to function). Considering the diameter of the borehole, the observed borehole deviation at the base of the inclinometer, and tilt angle of the sensors, it was considered that the sensor packages were installed without significant tilt and that sensors strings were separated laterally at equal distances from one another as shown in Table 4. The location of each sensor in the global coordinate system (i.e., relative to GPS-based East and West) was used to compute the velocities in baseline small-strain and blast-induced large strain excitations.

Table 2. Baseline zero-tilt gravitation observations for first MEMS in each module.

	Inclinometer Module							
Metric	1029	1030	1031	1032	1124	1125	1126	1127
Mean (g)	0.6240	0.6320	0.6360	0.6020	0.6230	0.6310	0.6160	0.6150
Standard deviation (g)	3.0E-04	2.7E-05	1.7E-05	5.4E-03	1.5E-04	5.4E-04	3.1E-05	7.8E-04
COV	0.047%	0.004%	0.003%	0.899%	0.023%	0.086%	0.005%	0.127%

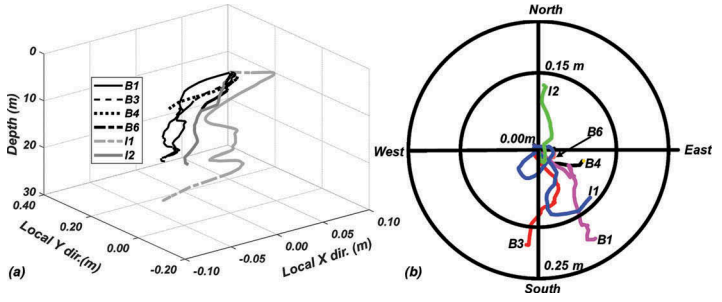

Figure 7. Deviation of each inclinometer casing within mud-rotary borings drilled to house various instruments: (a) lateral deviation beginning from the ground surface, and (b) plan view representation of deviation. Refer to Figure 3 for borehole locations.

Table 3. Summary of velocity transducer sensor package tilt deduced from the IMUs.

Tilt angle	Boring B6 (Depth, 12.50 m)			Boring B4 (Depth, 12.50 m)			Boring B3 (Depth, 27.43 m)			Boring B1 (Depth, 27.43 m)		
	S3	S4	S5	S6	S7	S8	S9	S10	S11	S12	S13	S14
Local *X* (°)	-0.6	-1.5	-1.9	2.18	-2.9	-1.9	NA	-3.5	NA	0.8	sNA	-3.5
Local *Y* (°)	-2.4	1.9	0.6	2.58	-0.2	-0.1	NA	-3.4	NA	-0.1	NA	-1.6

4.4 *As-built velocity transducer orientation*

Once installed, the geophone sensor packages were located (using methods described above), but the orientation of each geophone was unknown, and had to be determined prior to the blast experiments for corrections to the global East-West experiment alignment. Various methods exist for the determination of the in-ground orientation of geophones, including cross correlation (Zeng and McMechan 2006; Zha et al. 2013; Grigoli et al. 2012), assessment of particle motion (Trehu 1984), and polarization analysis (Jurkevics 1988; Zeng and McMechan 2006). Cross correlation requires the comparison of two geophones to determine the approximate angle between the sensor packages. In order to determine the as-installed orientation of the geophones at the test site, two approaches were selected: particle motions were used to determine the approximate orientation of the geophone sensor package in comparison to the shot location and type of hammer shot, whereas the summation of the root mean square errors (RMSE) was used to find the precise orientation after homing in on the approximate orientation.

Table 4. Summary of velocity transducer sensor locations relative to the top of each boring and the global coordinate (E-W) system.

Sensor Pair	Separated E-W distance (m)	Offset in N-S [N^+] (m)	Offset in E-W [E^+] (m)	Depth, *Z*, below ground surface [Z^+] (m)
B1: S12	2.484	-0.175	0.125	23.672
B3: S9		-0.226	-0.037	23.661
B1: S13	2.484	-0.177	0.135	24.891
B3: S10		-0.245	-0.039	24.882
B1: S14	2.484	-0.180	0.142	26.113
B3: S11		-0.264	-0.043	26.111
B4: S6	2.395	-0.013	0.110	8.991
B6: S3		0.027	0.037	9.003
B4: S7	2.395	-0.009	0.126	10.215
B6: S4		0.045	0.042	10.223
B4: S8	2.395	-0.005	0.141	11.440
B6: S5		0.060	0.047	11.451

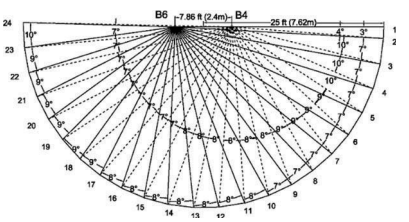

Figure 8. Array laid out for the shallow sensor packages using a radius of 7.62 m with shots spaced at approximately 1.07 m increments.

The use of particle motions was aided by shot arrays consisting of two semicircles with a radius 7.62 m and the center set between the borings housing the geophones (e.g., B4 and B6 in Figure 8) The radius was chosen so as to be larger than the *s*-wave wavelength, but small enough to provide a strong signal. Three shots on an aluminum plate and a shear beam and were used to generate compression and shear waves, respectively. Clear body waves in each geophone component were extracted from the data and plotted to assess peak amplitude relative to shot location. The approximate orientation of the geophone sensor packages was observed when a "strong" and "weak" motion was induced along and perpendicular to the plane of particle motion for a single shot location (Trehu, 1984). The particle motions are plotted in the *XY, XZ*, and *YZ* component directions of each sensor package so that a given shot can produce the maximum and minimum particle motion observed in two mutually perpendicular component planes (e.g., shots 2 and 14 for geophone package S3 in Figure 9). Following identification of approximate geophone component directions, additional shots were performed to improve the precision of the orientation.

Separately, the RMSE approach uses one cycle of the selected waveform from the dominant body wave motion to compute the resultant vector motion amplitude of a given shot. The observed amplitudes of two (near-perpendicular) motion components is subtracted from their vector resultant, R_T, multiplied by the cosine of the sum of the angle at which the shot was hammered, θ, and the proposed angle of deviation of the geophone, both referenced from the global East-West alignment, i. The RMSE in excitation amplitude is then computed using:

$$RMSE(i) = \sqrt{\sum_{t=1}^{T} \frac{((R_T cos(\theta + i) - x_t)^2}{T}} \tag{1}$$

where T is the number of data points in one cycle of the waveform, x_t is the velocity amplitude of observation in mV. Figure 10 depicts the sum of the RMSE for every shot plotted against i. The minimum values on the graph indicate the orientation of the sensor packages. The angles determined using the particle motion amplitudes are 3° and 92° from the East-West global alignment for the X and Y component respectively (Figures 1, 8, and 9). In comparison, the RMSE approach suggests that these components are oriented at 9° and 96° from the East-West global alignment (Figure 1, 8 and 10). The use of the two disparate methods confirm the general orientation of the geophone sensor packages, but indicate slight differences from one another and the lack of pure perpendicular orientation. These differences stem in part from: (1) differences in the accuracy of the methods, and (2) the deviation in the as-

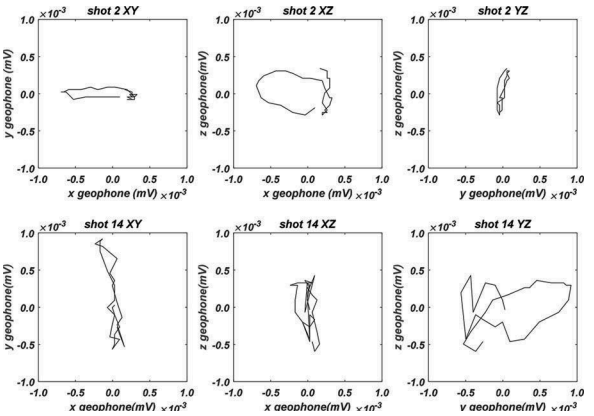

Figure 9. Plots of particle motion for the geophone sensor package S3, at orientations (Shots 2 and 4; see Figure 8) that produced their maximum X and Y component amplitudes.

built orientation of the geophones within the sensor package from 90°. In consideration of method accuracy, the RMSE approach was considered more robust and was used for subsequent analyses of downhole and crosshole geophysical testing and controlled blasting. Note that following determination of the geophone sensor package orientations, the polarity of each geophone in the sensor package was assessed using downhole shear wave velocity tests.

5 CONCLUDING REMARKS

Development of a comprehensive suite of site-specific parameters for seismic loading is necessary for design of critical infrastructure and lifelines. In some instances, retrieval of samples from soil deposits subject to strong ground motion may be difficult or costly. In-situ seismic testing offers an alternative means to evaluate the soil response to loading, and allows testing under existing stresses, drainage pathways, and with minimal soil disturbance. However, the planning, development, and calibration of the instrumentation necessary for conducting such tests requires careful attention to detail and proper assessment of post-installation response. This paper describes the steps necessary to sufficiently calibrate and assess the post-installation situation (e.g., lateral separation distance, orientation, tilt) of the suite of sensors comprising two in-situ test arrays. The depth of instrumentation posed particular challenges to assess separation distance, necessary for assessment of changes in crosshole velocity, and instrument orientation, necessary for resolving the components of velocity to the selected global test alignment. The procedures and protocols developed herein set the framework for future successful, deep, in-situ seismic testing of soils where such testing is deemed advantageous with regard to the available alternatives (ground freezing and laboratory testing of small samples).

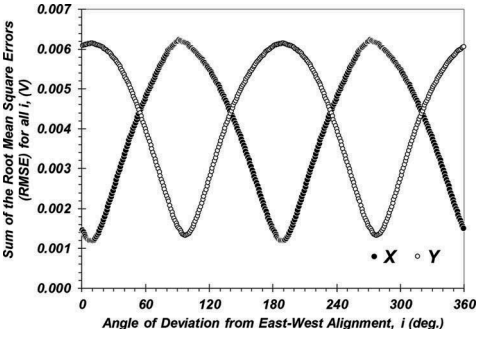

Figure 10. Root mean square error analysis for geophone sensor package, S3, located in Boring B6. The orientations of the *X* and *Y* components correspond to the minimum RMSEs.

ACKNOWLEDGEMENTS

This research was funded by the Cascadia Lifelines Program (CLiP) and the Port of Portland. This funding, as well as the significant leadership and assistance of Tom Wharton, P.E., is gratefully acknowledged.

REFERENCES

Atwater, B. F.; Musumi-Rokkaku, S.; Satake, K.; Yoshinobu, T.; Kazue, U.; Yamaguchi, D. K. 2005. The Orphan Tsunami of 1700—Japanese Clues to a Parent Earthquake in North America. *U.S. Geological Survey Professional Paper 1707*. Reston, VA, U.S. Geological Survey.

Cox, B.R. (2006). Development of a direct test method for dynamically assessing the liquefaction resistance of soils in situ. *PhD Thesis*, University of Texas at Austin, 498 pp.

Cox, B., Stokoe, K., and Rathje, E. 2009. An in -situ test method for evaluating the coupled pore pressure generation and nonlinear shear modulus behavior of liquefiable soils. *ASTM Geotechnical Testing Journal*: 32(1),11-21

Geodaq (2014). i6 Series In-Place Inclinometer. Geodaq, Inc., Sacramento, CA, 2 pp.

Gianella, T.N. and Stuedlein, A.W. 2017. Performance of Driven Displacement Pile-Improved Ground in Controlled Blasting Field Tests. *J. Geot. Geoenv. Eng.*: 143(9), 04017047

Goldfinger, C., Nelson, C. H., Morey, A., Johnson, J. E., Gutierrez-Pastor, J., Eriksson, A. T., Karabanov, E., Patton, J., Gracia, E., Enkin, R., Dallimore, A., Dunhill, G., and T. Vallier, 2012. Turbidite Event History: Methods and Implications for Holocene Paleoseismicity of the Cascadia Subduction Zone, *USGS Professional Paper 1661-F*, Reston, VA, U.S. Geological Survey, pp. 184.

Grigoli, F., Cesca, S., Dahm, T., and Krieger, L. 2012. A complex Linear Least-squares method to derive relative and absolute orientations of seismic sensors. *Geophysical J. Int.*: 188(3),1243-1254.

Jurkevics, A. 1988. Polarization Analysis of Three-Component Array Data. *Bul. Seis. Soc. Am.*: 78 (5),1725-1743.

Rollins, K. M., Lane, J. D., Dibb, E., Ashford, S. A., and Mullins, A. G. 2005. Pore pressure measurement in blast-induced liquefaction experiments. *Transportation Research Record*: 1936(1), pp. 210-220.

Trehu, A. (1984). Lateral velocity variations in the Orozco Transform Fault inferred from observed incident angles and azimuths of P-waves. *Geophysical J. Int.*: 77(3),711-728.

van Ballegooy, S., Roberts, J.N., Stokoe, K.H., Cox, B.R., Wentz, F.J., and Hwang, S. 2015. Large-Scale Testing of Shallow Ground Improvements using Controlled Staged-Loading with T-Rex. 2015. *6th Int. Conf. Earthquake Geotech. Eng.*, Christchurch, New Zealand, 10 pp.

Zeng, X., and McMechan, G. 2006. Two Methods for determining geophone orientations from VSP data. *Geophysics*: 71(4),V87-V97.

Zha, Y., Webb Spahr, and Menke, W. 2013. Determining the orientations of ocean bottom seismometers using ambient noise correlation, *Geophysical Research Letters*: 40(14) 1-6.